Journal of Power Sources 251 (2014) 325–330

Contents lists available at ScienceDirect

Journal of Power Sources

journal homepage: www.elsevier.com/locate/jpowsour

Short communication

Nanosized $LiVPO_4F$/graphene composite: A promising anode material for lithium ion batteries

Jiexi Wang, Xinhai Li*, Zhixing Wang, Bin Huang, Zhiguo Wang, Huajun Guo*

School of Metallurgy and Environment, Central South University, 932 South Lushan Road, Changsha 410083, PR China

HIGHLIGHTS

- First synthesis of nanosized $LiVPO_4F$/graphene (LVPF/G) composite.
- First introduction of LVPF/G as anode material.
- Altering the discharge cut-off potential to improve the performance of LVPF/G.
- Superior cycle ability and rate capability delivered by LVPF/G at 3.0 −0.01 V.

GRAPHICAL ABSTRACT

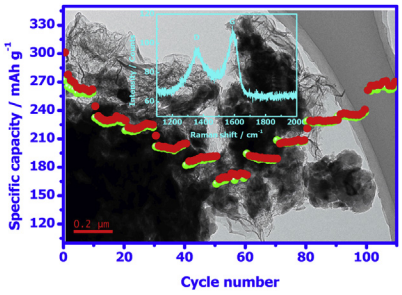

ARTICLE INFO

Article history:
Received 15 October 2013
Received in revised form
19 November 2013
Accepted 27 November 2013
Available online 7 December 2013

Keywords:
Lithium vanadium fluorophosphate
Graphene
Composite
Anode material
Lithium ion battery
Cut-off potential

ABSTRACT

This study first reports the synthesis of the nanosized $LiVPO_4F$/graphene composite (LVPF/G). The LVPF/G composite is prepared by a facile mechanochemical approach. XRD results reveal that the prepared composite are well crystallized with triclinic $LiVPO_4F$. SEM and TEM images demonstrate that the $LiVPO_4F$ nanoparticles in the composite are well enwrapped by graphene. Used as anode material for lithium ion batteries, the prepared LVPF/G composite exhibits greatly improved electrochemical performance. Furthermore, the electrochemical properties the LVPF/G composite depend heavily on the discharge cut-off potential. When the cut-off potential is altered to 0.01 V vs. Li/Li^+, it possesses the best electrochemical performance. Under such optimal charge−discharge condition (3−0.01 V vs. Li/Li^+), it shows an initial charge capacity of 287 mAh g^{-1} at 0.1C rate (1C = 310 mA g^{-1}) and shows no capacity fading after 100 cycles. It also exhibits good rate capability, delivering about 168 mAh g^{-1} at 10C rate.

1. Introduction

Rechargeable lithium ion batteries (LIBs) are the most promising candidates for advanced clean energy storage devices because of their high energy-storage density, long-term cycle life and ambient temperature operation [1,2]. As one of the components of LIBs, anode material play an important role in LIBs' operation. Carbon and its related materials (especially graphite) have been used as main anodes for commercial LIBs [3,4]. However, their relatively poor cycle performance and rate capability limit their applications in some special conditions. Furthermore, the low operating potential of lithiated graphite (LiC_6) would cause the deposition of dendritic lithium on the surface of anode, leading to safety concerns particularly in high-power equipment [5–7]. These drawbacks of conventional carbon materials have driven the researchers to develop the alternatives [8,9]. Transitional metal oxides and silicon-based materials with high capacities have been widely investigated to replace the currently used anodes [10]. However, the problems of high irreversible capacity and poor cycle

* Corresponding authors.
E-mail addresses: xinhaili_csu@126.com (X. Li), hjguo_csu@163.com (H. Guo).

0378-7753/$ – see front matter © 2013 Elsevier B.V. All rights reserved.
http://dx.doi.org/10.1016/j.jpowsour.2013.11.095

performance of these materials that rooted mainly in large volume change and low conductivity, should be solved before their application [11]. Therefore, it is necessary to continue developing potential anode candidates with stable structure, high safety, and good electrochemical performance.

$LiVPO_4F$ has been widely investigated as a potential cathode material for LIBs operating at 4.2 V vs. Li/Li^+ [12–18]. Interestingly, the redox reaction of V^{3+}/V^{2+} that occurs at 1.8 V vs. Li/Li^+, makes it possible to use $LiVPO_4F$ as anode material [19–23]. Recently, Shu and his group have investigated the possibility of increasing the capacity of $LiVPO_4F$ via lowering the discharge potential and the V^{2+}/V^+ redox reaction has been discovered when the discharge cut-off potential was 0 V vs. Li/Li^+ [6]. Under such low cut-off potential, the capacity of $LiVPO_4F$ could be increased to about 275 mAh g^{-1}. However, in this literature, the $LiVPO_4F$ showed unacceptable cycle performance and rate capability due to some drawbacks such as poor electronic conductivity and slightly irreversible structural evolution. Therefore, it is of great significance to develop an effective strategy to operate the $LiVPO_4F$ with high capacity, good cycle performance, as well as superior rate capability.

Graphene has become a spotlight in the field of energy conversion due to its superior electronic conductivity, large specific surface area, excellent structural flexibility and high surface to volume ratio [24,25]. In this report, we first introduce the synthesis of the nanosized $LiVPO_4F$/graphene composite (LVPF/G) by mechanochemical approach and its application as high-performance anode material for LIBs. Nanosized particles are able to provide short pathways for Li^+ ion transmission [11] and graphene can enhance the conductivity of the composite [24]. Compared with conventional two-step carbon thermal reduction (CTR) method [12] and sol–gel strategy [13,26], the mechanochemical approach is a more simple, facile and effective way to synthesize highly purified products [16,18,27]. We expect this nanostructured composite to display superior electrochemical properties including cycle performance and rate capability. The discharge cut-off potential is altered to achieve better performance of the prepared composite.

2. Experimental section

The graphene oxide was prepared by an improved hummers' method [28]. In this study, the final product was re-dispersed into the ethanol. The concentration of graphene oxide in the obtained solution is about 4 mg mL^{-1}.

The $LiVPO_4F$/graphene composite (LVPF/G) by mechanochemical approach [18,29,30]. All chemicals were purchased from Aladdin reagent (Shanghai) co., Ltd. Stoichiometric vanadium pentoxide (V_2O_5, 99.0 wt.%), ammonium dihydrogen phosphate ($NH_4H_2PO_4$, 99.0 wt.%), lithium fluoride (LiF, 98.5 wt.%), and 20% excess oxalic acid ($H_2C_2O_4 \cdot H_2O$, 99.5 wt.%) were dispersed into 50 mL diluted graphene oxide ethanol solution. Then the mixture reacted under ball milling (ND6-2L, 0.75 kW) for 8 h at room temperature with a revolving speed of 250 r min^{-1}. After that, the obtained slurry was dried overnight in the vacuum oven at 90 °C. Finally, the dried powers were annealed first at 300 °C for 2 h and then at 700 °C for 6 h in a tube furnace under argon atmosphere.

Samples without adding graphene and extra carbon (LVPF) and with the similar amount of carbon to that in LVPF/G (LVPF/C) were prepared in the same route for comparison. The LVPF was prepared by using alcohol, in place of graphene oxide ethanol solution, as dispersing agent during the ball milling process. The LVPF/C was synthesized in the similar method to the preparation of LVPF except that the conductive carbon black was added before ball milling process. The carbon content in LVPF/C was controlled to near to that in LVPF/G.

The powder X-ray diffraction (XRD, Rint-2000, Rigaku, Japan) using Cu Kα radiation was employed to identify the crystalline phase of the prepared samples. The morphologies of the prepared samples were observed by scanning electron microscope (SEM, JEOL, JSM-5612LV) with an accelerating voltage of 20 kV, and by transmission electron microscope (TEM, Tecnai G12, 200 kV). The Raman spectra of the prepared sample from 50 to 2000 cm^{-1} were obtained from WiTec Alpha300 system applying 632.8 nm laser light. Carbon content in the samples was determined by C–S analysis equipment (Eltar, Germany).

The electrochemical characterizations were evaluated using CR2025 coin-type cell. The working electrodes were prepared by mixing the LVPF powders with 10 wt.% acetylene black and 10 wt.% polyvinylidene fluoride in N-methyl pyrrolidinone until slurry was obtained. Then, the blended slurry was pasted onto an Cu foil current collector and dryed 120 °C for 12 h. After that, it was cut into rounded pieces with an area of 1.13 cm^2. The active material on each piece weighs about 1.2 mg. Lithium foil was used as counter

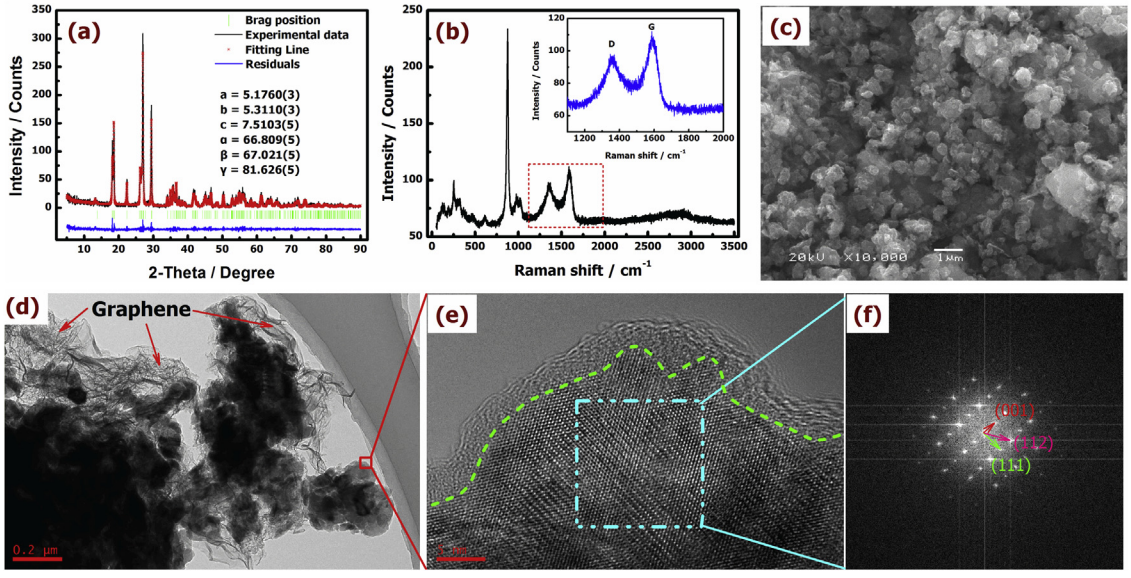

Fig. 1. (a) XRD pattern, (b) Raman spectra, (c) SEM image, (d) TEM image, (e) HRTEM image and (f) FFT image of LVPF/G.

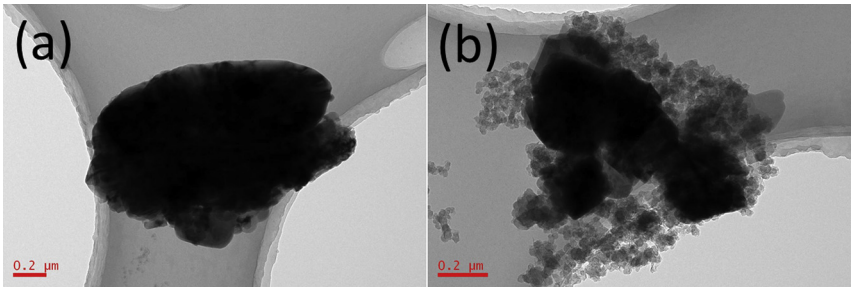

Fig. 2. TEM images of (a) LVPF and (b) LVPF/C.

electrode and reference electrode. a porous polypropylene film was used as separator. The electrolyte was 1 mol L^{-1} $LiPF_6$ in EC, EMC and DMC (1:1:1 in volume). The assembly of the cells was carried out in a dry Ar-filled glove box. Galvanostatic charge–discharge tests were carried out using NEWARE battery circler, in the voltage range of 3.0–1.0, 3.0–0.5, 3.0–0.01 V vs. Li/Li^+ at room temperature. The electrochemical impedance spectroscopy (EIS) measurements were carried out with a CHI660D electrochemical analyzer by applying an AC voltage of 5 mV amplitude in the 0.01 Hz–100 kHz frequency range.

3. Results and discussion

Fig. 1(a) shows the XRD pattern of the prepared LVPF/G. All peaks are indexed with that of triclinic $LiVPO_4F$ with the space group of P-1. No impurity peak of $Li_3V_2(PO_4)_3$ is found. The Rietveld refinement of the XRD data are performed with Program Maud using the standard data (20808-ICSD) and the refined cell parameters are $a = 0.51760(3)$ nm, $b = 0.53110(3)$ nm, $c = 0.75103(5)$ nm, $\alpha = 66.809(5)^\circ$, $\beta = 67.021(5)^\circ$, $\gamma = 81.626(5)^\circ$, which are similar to that in other reports [31,32]. There is no obvious peak of graphite in the XRD pattern, indicating the carbon in the prepared composite is amorphous. The carbon content in the composite is determined to be 6.4 wt.%. Raman spectra is recorded to prove the existence of reduced graphene oxide. As seen in Fig. 1(b), two peaks are observed at ~1360 and ~1588 cm^{-1}, which correspond to the A_{1g} mode of disordered carbon (D-band) and the Raman active E_{2g} mode of the graphitic carbon lattice vibration (G-band), respectively. The I_D/I_G ratio of 0.875 reveals the existence of graphene (disordered graphite) in the composite [33]. Weak peaks at 2700-3200 cm^{-1} are also observed, which can be assigned to the characteristic peaks of reduced graphene oxide [34,35]. SEM image in Fig. 1(c) shows that the fine $LiVPO_4F$ particles with particle size of about hundreds of nanometers, are coexisted with graphene films. TEM and HRTEM analyses are conducted for further studying the morphology of LVPF/G. In Fig. 1(d), it can be clearly seen that the $LiVPO_4F$ primary particles with dozens of nanometers are homogeneously distributed into the graphene frameworks. HRTEM image in Fig. 1(e) shows that the crystalline $LiVPO_4F$, which is identified by the Fast-Fourier-Transition (FFT) in Fig. 1(f), is

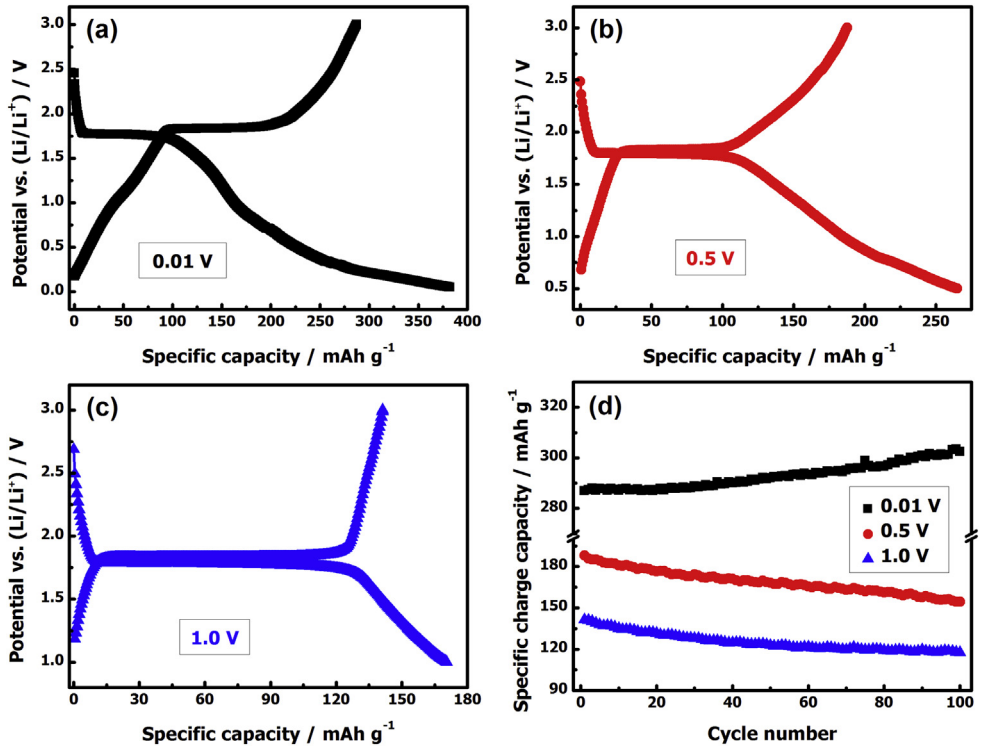

Fig. 3. Initial discharge–charge curves of LVPF/G at 0.1C under different discharge cut-off potentials vs. Li/Li^+: (a) 0.01 V, (b) 0.5 V, (c) 1.0 V; (d) Cycle performance of LVPF/G at 0.1C at different discharge cut-off potentials.

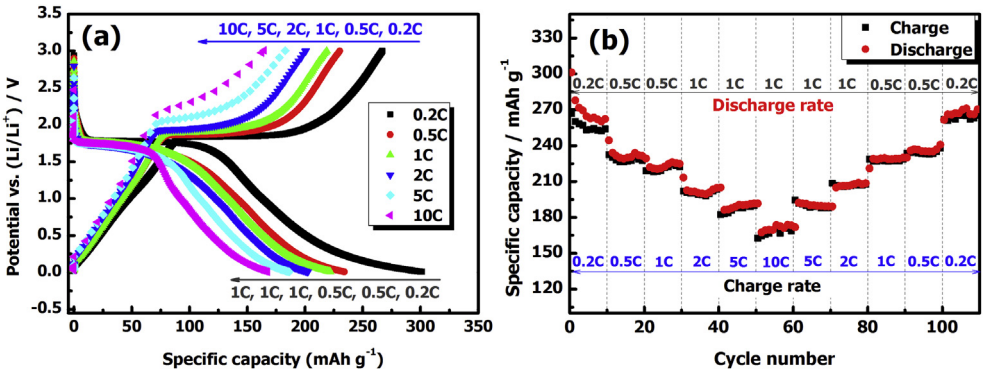

Fig. 4. (a) Initial discharge–charge curves and (b) specific capacities of LVPF/G at different artificially controlled current densities.

surrounded by an amorphous graphene layer. Fig. 2 shows the microstructures of the prepared LVPF and LVPF/C. As seen in Fig. 2(a), the particles in LVPF are bare and no obvious coating is observed on the surface of the particles. Moreover, the particle size of LVPF is larger than that of LVPF/G due to agglomeration. In Fig. 2(b), the $LiVPO_4F$ crystals in LVPF/C are surrounded loosely by dispersive carbon nanoparticles. The carbon contents of LVPF and LVPF/C are 1.1 and 6.7 wt.%, respectively. The carbon in LVPF comes from the pyrolysis of the excess oxalic acid. Compared to morphologies of LVPF and LVPF/C, the architecture of the LVPF/G composite is preponderant, which may lead to greatly improved Li^+ ion and electronic conductivity of LVPF/G and thus enhance the electrochemical performance.

The electrochemical performances of LVPF/G are investigated in CR2025 cells at room temperature by altering the discharge cut-off potential. Fig. 3(a)–(c) shows the initial discharge–charge curves of LVPF/G at 0.1C rate (1C = 310 mA g^{-1}) in the potential range of 3.0–0.01, 3.0–0.5, 3.0–1.0 V vs. Li/Li^+, respectively. As show in Fig. 3(a)–(c), the capacity of the composite increases with decreasing the discharge cut-off potential, which is due to Li^+ further insertion/extraction into/out of $Li_{2+x}VPO_4F$ ($0 < x < 1$) at lower potential [6]. The graphene can also contribute to improving the capacity [36]. The initial specific charge capacities of the LVPF/G at 0.1C rate are 287, 188, 141 mAh g^{-1} under the discharge cut-off potentials of 0.01, 0.5, 1.0 V vs. Li/Li^+, with the coulombic efficiencies of 72.2, 75.2, 82.9%, respectively. When the cut-off potential is lowered, the cell shows enlarged initial irreversible capacity, which is due to the formation of solid electrolyte interface (SEI) film [37–39] and slightly irreversible structural evolution of $LiVPO_4F$ [6]. Great difference in cycling ability is found in Fig. 3(d). As the cycling goes on, the capacities decrease in the cells discharged to 0.5, 1.0 V, with the capacity retentions of 81.9, 83.6% after 100 cycles, respectively. In contrast, the cell at the discharge cut-off potential of 0.01 V shows no capacity fading and even a little increase.

Fig. 4 shows the rate capability of LVPF/G. It can be seen in Fig. 4(a) that, as the current increases from 0.2 to 10C, the prepared

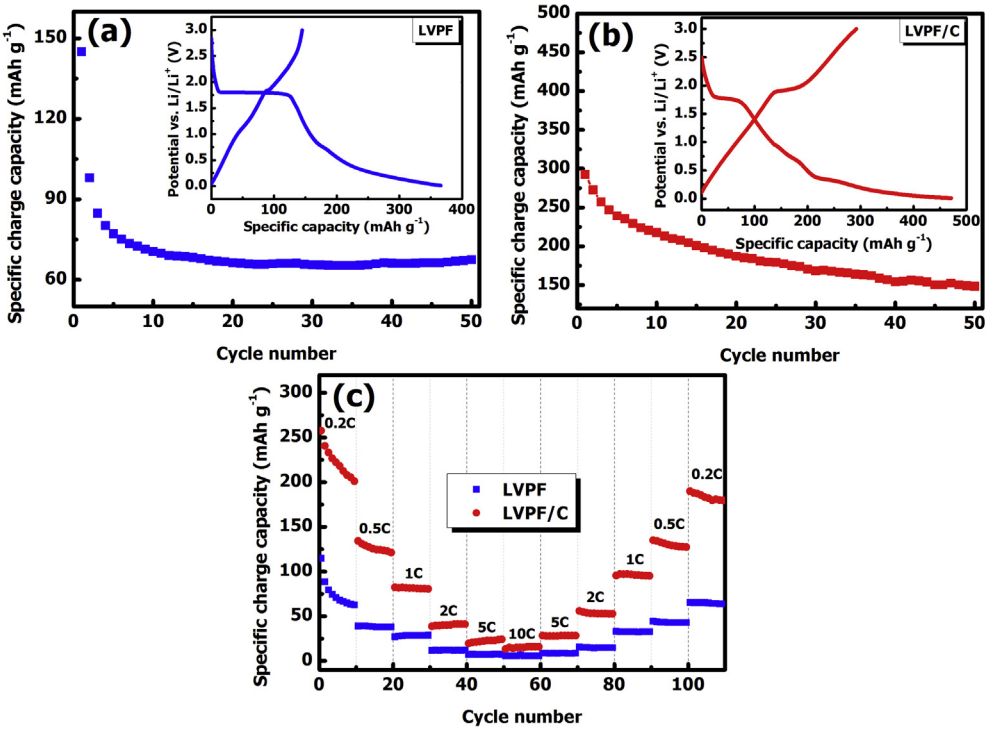

Fig. 5. Initial discharge–charge curves (inset) and cycle performance of (a) LVPF and (b) LVPF/C, (c) rate capability of LVPF and LVPF/C.

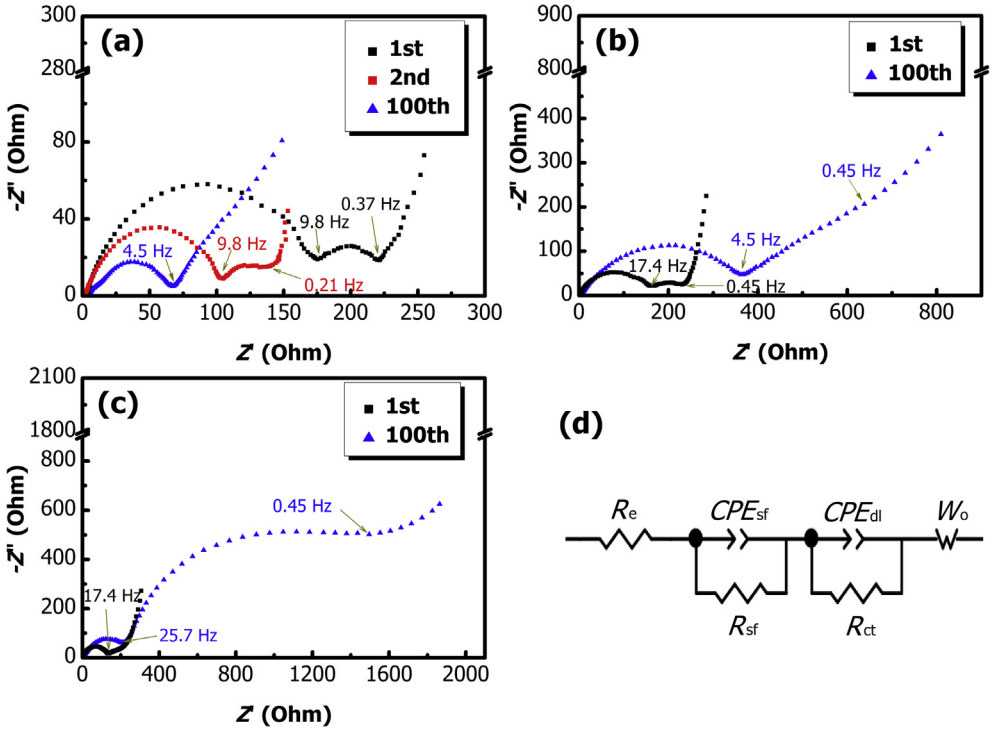

Fig. 6. Nyquist plots of LVPF/G in the 1st and 100th cycle at the corresponding discharge states: (a) 0.01 V, (b) 0.5 V, (c) 1.0 V vs. Li/Li$^+$, (d) equivalent circuit that used to fit the EIS data.

composite shows some degree of capacity fading from 267 to 168 mAh g^{-1}. More than half capacity is maintained when the current density is enlarged ten times. As observed in Fig. 4(b), the cell at 0.2C after cycling at higher current densities shows almost no obvious capacity fading, indicating good capacity recovery under the artificially controlled unstable discharge–charge current densities.

In order to emphasize the superior electrochemical performance of LVPF/G, the results of electrochemical performance of LVPF and LVPF/C are presented in Fig. 5. In Fig. 5(a) and (b), the LVPF and LVPF/C deliver an initial discharge capacity of 366, 471 mAh g^{-1} and charge capacity of 145, 292 mAh g^{-1}, with low coulombic efficiencies of 39.6%, 61.9%, respectively. After 50 cycles, the LVPF and LVPF can only maintain 46.9% and 50.7% capacity retention, respectively. As can be seen in Fig. 5(c), both samples show poor rate capability, exhibiting the capacity as low as ~10 mAh g^{-1} when the charge current of 10C is applied.

It can be easily concluded that the electrochemical performance of LVPF/G is much better than that of LVPF and LVPF/C. The superior electrochemical performance of LVPF/G is attributed to the ideal architecture of $LiVPO_4F$ nanoparticles and highly-dispersed graphene in the composite. On the one hand, since the $LiVPO_4F$ particles are nanosized, they can shorten the Li$^+$ ion transmission passageways. On the other hand, the graphene owns good electronic conductivity and is able to provide conductive framework for the composite. As a result, the electrochemical performance including in cycling ability and rate capability of LVPF/G is significantly improved by the enhanced electron and Li$^+$ ion transmission capability of the composite. Furthermore, the graphene have been proved to exhibit Li$^+$ ion storage capacity up to 1100 mAh g^{-1} [35] and can improve the capacity of the LVPF/G composite.

For further investigating the effect of discharge cut-off potential on the electrochemical performance of LVPF/G, the electrochemical impedance spectroscopy (EIS) is conducted in different cycle number at the corresponding discharge states. The Nyquist plots (Fig. 6(a)–(c)) are fitted with the equivalent circuit as show in Fig. 6(d), and fitted results are shown in Table 1, respectively. Two semicircles, which separately correspond to the surface-film (R_{sf}) and charge-transfer (R_{ct}) impedances [14,40], are observed in the EIS spectra. As seen in Fig. 6(a), when the discharge cut-off potential is 0.01 V vs. Li/Li$^+$, the R_{sf} value decreases dramatically while the R_{ct} value shows no obvious change as the cycling goes on. In contrast, when the discharge cut-off potential is 0.5 (Fig. 6(b)) and 1.0 V (Fig. 6(c)) vs. Li/Li$^+$, both the R_{sf} and R_{ct} values are enlarged greatly. The difference in electrochemical impedance reflects the cycling performance difference of LVPF/G at the different discharge cut-off potentials, and the LVPF/G at the discharge cut-off potential of 0.01 V vs. Li/Li$^+$ show decreased surface-film resistance and relatively stable charge-transfer resistance, possibly leading to much better cycling ability than that at the discharge cut-off potential of 0.5 V, 1.0 V vs. Li/Li$^+$.

Table 1
Fitted R_{sf}, R_{ct} values of LVPF/G in the 1st and 100th cycle at the corresponding discharge states.

Sample state	0.01 V			0.5 V		1.0 V	
	1st	2nd	100th	1st	100th	1st	100th
R_{sf} (±Ω)	160	100	6	140	357	118	203
R_{ct} (±Ω)	64	41	51	88	611	69	1101

4. Conclusions

The $LiVPO_4F$/graphene nanocomposite (LVPF/G) was successfully prepared by a facile mechanochemical route using diluted graphene oxide ethanol solution as dispersing agent for the first time. The nanosized primary particles were well coated by and distributed in the highly-dispersed graphene, and the aggregations

of $LiVPO_4F$ were also enwrapped by graphene. The electrochemical performance of LVPF/G anode depended heavily on the discharge cut-off potential. At the optimal charge–discharge condition (3.0–0.01 V vs. Li/Li^+), the prepared LVPF/G composite exhibited superior electrochemical performance including in cycling ability and rate capability, which could be attributed to the aforementioned ideal architecture of the composite that owned remarkably enhanced capability of Li^+ ion and electronic transmission. The improvement on electrochemical performance provided the possibility to develop $LiVPO_4F$ as a promising high-performance anode material.

Acknowledgments

This work was financially supported by the National Basic Research Program of China (973 Program, 2014CB643406), Major Special Project of Science and Technology of Hunan Province, China (No. 2011FJ1005), and Hunan Provincial Innovation Foundation for Postgraduate.

References

[1] L. Lu, X. Han, J. Li, J. Hua, M. Ouyang, J. Power Sources 226 (2013) 272–288.
[2] J.M. Tarascon, Philos. T. Roy. Soc. A 368 (2010) 3227–3241.
[3] L. Qie, W.M. Chen, Z.H. Wang, Q.G. Shao, X. Li, L.X. Yuan, X.L. Hu, W.X. Zhang, Y.H. Huang, Adv. Mater 24 (2012) 2047–2050.
[4] C. de las Casas, W. Li, J. Power Sources 208 (2012) 74–85.
[5] D. Aurbach, A. Zaban, Y. Ein-Eli, I. Weissman, O. Chusid, B. Markovsky, M. Levi, E. Levi, A. Schechter, E. Granot, J. Power Sources 68 (1997) 91–98.
[6] R. Ma, L. Shao, K. Wu, M. Shui, D. Wang, J. Pan, N. Long, Y. Ren, J. Shu, ACS Appl. Mater. Interfaces 5 (2013) 8615–8627.
[7] T.F. Yi, Y. Xie, Y.R. Zhu, R.S. Zhu, H.Y. Shen, J. Power Sources 222 (2013) 448–454.
[8] M.K. Datta, P.N. Kumta, J. Power Sources 165 (2007) 368–378.
[9] J.H. Lee, W.J. Kim, J.Y. Kim, S.H. Lim, S.M. Lee, J. Power Sources 176 (2008) 353–358.
[10] M.V. Reddy, G.V. Subba Rao, B.V. Chowdari, Chem. Rev. 113 (2013) 5364–5457.
[11] H.B. Wu, J.S. Chen, H.H. Hng, X.W.D. Lou, Nanoscale 4 (2012) 2526–2542.
[12] J. Barker, M.Y. Saidi, J.L. Swoyer, J. Electrochem. Soc. 150 (2003) A1394–A1398.
[13] Y. Li, Z. Zhou, X.P. Gao, J. Yan, J. Power Sources 160 (2006) 633–637.
[14] M.V. Reddy, G.V. Subba Rao, B.V.R. Chowdari, J. Power Sources 195 (2010) 5768–5774.
[15] X. Qiao, J. Yang, Y. Wang, Q. Chen, T. Zhang, L. Liu, X. Wang, J. Solid State Electr 16 (2012) 1211–1217.
[16] J.-c. Zheng, B. Zhang, Z.-h. Yang, J. Power Sources 202 (2012) 380–383.
[17] X. Sun, Y. Xu, M. Jia, P. Ding, Y. Liu, K. Chen, J. Mater. Chem. A 1 (2013) 2501–2507.
[18] J. Wang, X. Li, Z. Wang, H. Guo, Y. Zhang, X. Xiong, Z. He, Electrochim. Acta 91 (2013) 75–81.
[19] J. Barker, R.K.B. Gover, P. Burns, A. Bryan, Electrochem. ST. Lett. 8 (2005) A285–A287.
[20] J.M.A. Mba, L. Croguennec, N.I. Basir, J. Barker, C. Masquelier, J. Electrochem. Soc. 159 (2012) A1171–A1175.
[21] N.V. Kosova, E.T. Devyatkina, A.B. Slobodyuk, A.K. Gutakovskii, J. Solid State Electr (2013), http://dx.doi.org/10.1007/s10008-013-2213-1.
[22] J.M.A. Mba, C. Masquelier, E. Suard, L. Croguennec, Chem. Mater 24 (2012) 1223–1234.
[23] B.L. Ellis, T.N. Ramesh, L.J.M. Davis, G.R. Goward, L.F. Nazar, Chem. Mater 23 (2011) 5138–5148.
[24] Z.-S. Wu, G. Zhou, L.-C. Yin, W. Ren, F. Li, H.-M. Cheng, Nano Energy 1 (2012) 107–131.
[25] L. Chen, M. Zhang, W. Wei, J. Nanomater 2013 (2013) 1–8.
[26] S.-k. Zhong, W. Chen, Y.-h. Li, Z.-g. Zou, C.-j. Liu, T. Nonferr. Metal. Soc 20 (2010) s275–s278.
[27] J.C. Zheng, X.H. Li, Z.X. Wang, S.S. Niu, D.R. Liu, L. Wu, L.J. Li, J.H. Li, H.J. Guo, J.Power Sources 195 (2010) 2935–2938.
[28] W.S. H Jr., R.E. Offeman, J. Am. Chem. Soc 80 (1958) 1339.
[29] J. Wang, X. Li, Z. Wang, H. Guo, Y. Li, Z. He, B. Huang, J. Alloy. Compd 581 (2013) 836–842.
[30] J. Wang, Z. Wang, X. Li, H. Guo, X. Wu, X. Zhang, W. Xiao, Electrochim. Acta 87 (2013) 224–229.
[31] J. Barker, R.K.B. Gover, P. Burns, A. Bryan, M.Y. Saidi, J.L. Swoyer, J. Power Sources 146 (2005) 516–520.
[32] J. Wang, Z. Wang, X. Li, H. Guo, W. Xiao, S. Huang, Z. He, J. Solid State Electr 17 (2013) 1–8.
[33] M.S. Dresselhaus, A. Jorio, M. Hofmann, G. Dresselhaus, R. Saito, Nano Lett. 10 (2010) 751–758.
[34] Y.H. Jung, C.H. Lim, D.K. Kim, J. Mater. Chem. A 1 (2013) 11350–11354.
[35] B. Lung-Hao Hu, F.Y. Wu, C.T. Lin, A.N. Khlobystov, L.J. Li, Nat. Commun 4 (2013) 1687.
[36] S.Y. Han, I.Y. Kim, K.Y. Jo, S.-J. Hwang, J. Phys. Chem. C 116 (2012) 7269–7279.
[37] X. Chen, N. Zhang, K. Sun, J. Mater. Chem. 22 (2012) 15080–15084.
[38] C.K. Chan, R. Ruffo, S.S. Hong, Y. Cui, J. Power Sources 189 (2009) 1132–1140.
[39] K. Edström, M. Herstedt, D.P. Abraham, J. Power Sources 153 (2006) 380–384.
[40] M.V. Reddy, S. Madhavi, G.V. Subba Rao, B.V.R. Chowdari, J. Power Sources 162 (2006) 1312–1321.